

Article

# High-Coercivity Ferrimagnet $\text{Co}_2\text{FeO}_2\text{BO}_3$ : XMCD Insights into Charge-Ordering and Cation Distribution

Mikhail S. Platonov 

Synchrotron Radiation Facility SKIF, Kol'tsovo 630559, Russia; m.s.platonov@srf-skif.ru

**Abstract:** The multi-sublattice ferrimagnet  $\text{Co}_2\text{FeO}_2\text{BO}_3$ , a prominent example of lanthanide-free magnets, was the subject of element-selective studies using X-ray magnetic circular dichroism (XMCD) observations at the *L*- and *K*-X-ray absorption edges. Research findings indicate that the distinct magnetic characteristics of  $\text{Co}_2\text{FeO}_2\text{BO}_3$ , namely its remarkable high coercivity (which surpasses 7 Tesla at low temperatures), originate from an atypical arrangement of magnetic ions in the crystal structure (sp.gr. *Pbam*). The antiferromagnetic nature of the  $\text{Co}^{2+}$ -O- $\text{Fe}^{3+}$  exchange interaction was confirmed by identifying the spin and orbital contributions to the total magnetization from Co ( $m_L = 0.27 \pm 0.1 \mu_B/\text{ion}$  and  $m_S^{\text{eff}} = 0.53 \pm 0.1 \mu_B/\text{ion}$ ) and Fe ( $m_L = 0.05 \pm 0.1 \mu_B/\text{ion}$  and  $m_S^{\text{eff}} = 0.80 \pm 0.1 \mu_B/\text{ion}$ ) ions through element-selective XMCD analysis. Additionally, the research explicitly revealed that the strong magnetic anisotropy is a result of the significant unquenched orbital magnetic moment of Co, a feature that is also present in the related compound  $\text{Co}_3\text{O}_2\text{BO}_3$ . A complex magnetic structure in  $\text{Co}_2\text{FeO}_2\text{BO}_3$ , with infinite  $\text{Co}^{2+}\text{O}_6$  layers in the *bc*-plane and strong antiferromagnetic coupling through  $\text{Fe}^{3+}$  ions, is suggested by element-selective hysteresis data, which revealed that  $\text{Co}^{2+}$  ions contribute both antiferromagnetic and ferromagnetic components to the total magnetization. The findings underline the suitability of  $\text{Co}_2\text{FeO}_2\text{BO}_3$  for applications in extreme environments, such as low temperatures and high magnetic fields, where its unique magnetic topology and anisotropy can be harnessed for advanced technologies, including materials for space exploration and quantum devices. This XMCD study opens the door to the production of novel high-coercivity, lanthanide-free magnetic materials by showing that targeted substitution at specific crystallographic sites can significantly enhance the magnetic properties of such materials.



Academic Editor: Marius Andruh

Received: 18 November 2024

Revised: 17 December 2024

Accepted: 13 January 2025

Published: 15 January 2025

**Citation:** Platonov, M.S.High-Coercivity Ferrimagnet  $\text{Co}_2\text{FeO}_2\text{BO}_3$ : XMCD Insights into Charge-Ordering and Cation Distribution. *Inorganics* **2025**, *13*, 24. <https://doi.org/10.3390/inorganics13010024>

**Copyright:** © 2025 by the author. Licensee MDPI, Basel, Switzerland. This article is an open access article distributed under the terms and conditions of the Creative Commons Attribution (CC BY) license (<https://creativecommons.org/licenses/by/4.0/>).

**Keywords:** magnetism; coercive field; element-specificity; orbital-specificity; charge ordering

## 1. Introduction

Permanent magnets play a crucial role in modern technologies, ranging from electronic devices to renewable energy sources [1,2]. Although significant advancements have been made in developing powerful magnets like  $\text{Nd}_2\text{Fe}_{14}\text{B}$  and  $\text{SmCo}_5$ , progress in creating new permanent magnets with enhanced properties has slowed. This slowdown is partly due to concerns about the availability and environmental impact of lanthanides, which has increased interest in alternative materials such as strontium ferrites [3] and single-molecule [4–6] and single-chain magnets [7,8]. Researchers are particularly focused on developing lanthanide-free hard magnets using charge-ordering phenomena [9], which stabilize magnetic nanodomains and enhance resistance to demagnetization. One promising area of research involves multi-component systems, such as transition metal oxyborates like  $\text{M}^{2+}_2\text{M}^{3+}\text{O}_2\text{BO}_3$  with the mineral ludwigite structure (sp. gr. *Pbam*),

where M represents a transition metal or a metalloid. These materials exhibit charge-ordering properties [10–18] and show potential for creating magnets with high coercive force and magnetic anisotropy [13,19,20]. Additionally, their ability to operate in extreme environments, such as low temperatures and high magnetic fields, makes them particularly suitable for studying fundamental quantum cooperative phenomena like Bose–Einstein condensation, exotic magnetism, and spin-density waves.

$\text{Fe}_3\text{O}_2\text{BO}_3$  and  $\text{Co}_3\text{O}_2\text{BO}_3$  are the only known homometallic ludwigites, recognized for their complex magnetic behaviors, primarily due to their crystal structures, which contain four non-equivalent crystallographic sites. In  $\text{Fe}_3\text{O}_2\text{BO}_3$ , multiple transitions take place, including a structural transformation at  $T_S = 283$  K, where  $\text{Fe}^{2+}$  and  $\text{Fe}^{3+}$  ions pair up to form dimers in a 4–2–4 triad configuration ( $\text{Fe}^{3+}—\text{Fe}^{2+}—\text{Fe}^{3+}$  bound charge states) [10,21]. This structural change leads to antiferromagnetic (AFM) ordering at  $T_N = 112$  K. As the temperature decreases further, the material transitions to ferromagnetic chains in a 3–1–3 spin ladder at  $T = 74$  K [12], and finally to an AFM state at  $T = 30$  K [22,23]. In this low-temperature AFM phase, the direction of magnetic anisotropy transitions from the **a**-axis to the **b**-axis, with the coercive force reaching a peak of approximately 3 T at  $T = 35$  K.

In contrast,  $\text{Co}_3\text{O}_2\text{BO}_3$  exhibits typical behavior, characterized by a single ferrimagnetic transition at  $T_N = 42$  K along the **b**-axis. This transition is characterized by high uniaxial magnetic anisotropy and a coercive field of  $\sim 2$  T at  $T = 2$  K [11,22,24–26]. Replacing nonmagnetic  $\text{Co}^{3+}$  ions in  $\text{Co}_3\text{O}_2\text{BO}_3$  with magnetic  $\text{Fe}^{3+}$  ions to create  $\text{Co}_2\text{FeO}_2\text{BO}_3$  significantly alters its magnetic properties. This replacement results in a twofold increase in the ferrimagnetic transition temperature, reaching  $T_{N2} = 70$  K, and additionally brings about an AFM transition at  $T_{N1} = 115$  K along the **b**-axis [13,19,20,27]. Replacing nonmagnetic  $\text{Co}^{3+}$  ions with magnetic  $\text{Fe}^{3+}$  ions leads to a threefold reduction in remanent magnetization (from  $M_r = 3.5 \mu_B/\text{f.u.}$  to  $M_r = 1.1 \mu_B/\text{f.u.}$ ), attributed to antiferromagnetic interactions between Co and Fe. At the same time, the material's magnetic hardness is enhanced, producing coercive fields exceeding 7 T at temperatures below 15 K [25]. The combination of high magnetic anisotropy and unique cation distribution in  $\text{Co}_2\text{FeO}_2\text{BO}_3$  makes it a key material for applications requiring resilience to extreme magnetic and thermal conditions, such as resilient electronics for space missions or materials for high-pressure physics. Recent DFT + GGA calculations show that high-spin  $\text{Fe}^{3+}$  occupies crystallographic site 4, while high-spin  $\text{Co}^{2+}$  occupies sites 1, 2, and 3 [27]. This unusual cation distribution in  $\text{Co}_2\text{FeO}_2\text{BO}_3$  plays a critical role in altering its magnetic topology.

We utilized polarization-dependent X-ray absorption spectroscopy (XAS) to investigate the significant increase in magnetic properties of  $\text{Co}_2\text{FeO}_2\text{BO}_3$ . By focusing on the charge and magnetic characteristics of the Co and Fe ions, this study aimed to uncover the underlying mechanisms driving these enhancements in magnetic behavior. Compared to conventional techniques, X-ray magnetic circular dichroism (XMCD) [28] offers a unique advantage by providing element-specific insights into spin and orbital contributions to magnetization. This capability allows for precise identification of the magnetic interactions driving phenomena such as coercivity and magnetic anisotropy, which are critical for the development of advanced lanthanide-free magnets. These findings not only advance the understanding of low-dimensional magnetism in complex systems but also contribute to broader efforts in the discovery of quantum states of matter under extreme conditions.

## 2. Experimental Details

High-quality  $\text{Co}_2\text{FeO}_2\text{BO}_3$  single crystals were grown using a flux melt technique based on bismuth trimolybdate, following the method detailed in [19]. This approach ensures that  $\text{Bi}_2\text{O}_3$  and  $\text{MoO}_3$  effectively prevent the incorporation of Bi into the crystal structure, enabling the formation of well-defined crystals. The flux melt, composed

of  $\text{Bi}_2\text{Mo}_3\text{O}_{12}$  and  $\text{B}_2\text{O}_3$ , has low melting temperatures (643 °C for  $\text{Bi}_2\text{Mo}_3\text{O}_{12}$  and 450 °C for  $\text{B}_2\text{O}_3$ ) and low viscosity, facilitating the growth of large needle-shaped crystals (2–5 mm).  $\text{B}_2\text{O}_3$  ensures efficient dissolution of oxides. A mixture of 50 g of reactants ( $\text{Bi}_2\text{Mo}_3\text{O}_{12}:\text{B}_2\text{O}_3:\text{CoO}:\text{Na}_2\text{CO}_3:\text{Fe}_2\text{O}_3 = 3:2:4:3:3$ ) was heated in a platinum crucible at 900–1000 °C. The components were melted sequentially, with  $\text{Na}_2\text{CO}_3$  added last due to its decomposition at high temperatures. After homogenization at 1100 °C for 3 h, the temperature was reduced to 960 °C and cooled slowly. The resulting crystals were separated using 20% nitric acid. Black, rectangular prisms approximately 2.5 mm long and 50 microns wide were selected for the experiments. X-ray diffraction analysis was then performed using a Bruker SMART APEX II diffractometer (MoK $\alpha$  radiation, CCD detector) to determine the crystal structure. Magnetization measurements were taken using a Quantum Design PPMS 6000 vibrating sample magnetometer. Static magnetization measurements were performed in the temperature range of 2–300 K, and magnetization curves were obtained in magnetic fields up to 9 T. Prior to the measurements, the single crystal was accurately weighed using DV 215 CD microbalances. The single crystal, oriented with the aid of an X-ray diffractometer, was mounted on a plexiglass holder to ensure the magnetic field was sequentially aligned along each of the crystallographic axes. For each direction, dependencies of magnetization on temperature and magnetic field were recorded. For measurements along the crystallographic **b**-axis, the demagnetization effect due to the sample shape was evaluated. Taking into account uncertainties arising from weighing, holder signal subtraction, and measurements, the overall error in determining the sample magnetization did not exceed 5%. Soft X-ray measurements ( $L_{3,2}$ -edges of 3d metals and *K*-edge of O) were carried out at the UE46-PGM1 beamline at BESSY II in Berlin. Additionally, hard X-ray measurements (*K*-edges of Co and Fe) were performed at the ESRF ID12 beamline in Grenoble. Both experiments utilized the same oriented sample and were performed under varying temperatures and magnetic fields, offering a detailed understanding of the magnetic properties.

### 3. Results and Discussion

$\text{Co}_2\text{FeO}_2\text{BO}_3$  was determined to crystallize in the orthorhombic *Pbam* space group, and the measured unit cell parameters align closely with values reported in earlier research [19]. Specifically, the unit cell parameters are as follows:  $a = 9.3818(16)$  Å,  $b = 12.344(2)$  Å,  $c = 3.0578(5)$  Å,  $\alpha = \beta = \gamma = 90^\circ$ .

Ludwigite minerals exhibit structural features characterized by chains of metal ions in octahedral coordination across four non-equivalent crystallographic sites (1, 2, 3, and 4). These chains create a zigzag pattern along the *c*-axis, linked by trigonal  $\text{BO}_3$  units and shared oxygen atoms (Figure 1). In  $\text{Co}_3\text{O}_2\text{BO}_3$ , divalent ions predominantly occupy sites 1, 2, and 3, whereas trivalent ions are mainly situated at site 4, positioned among the  $\text{BO}_3$  groups [26]. This specific arrangement leads to a compact structure comprising alternating layers of divalent and trivalent ions, supporting charge-ordered configurations. Below 300 K, Co-O interionic distances remain stable, with  $\langle\text{Co4-O}\rangle$  being significantly shorter at 1.962(2) Å compared to  $\langle\text{Co1-O}\rangle$  (2.094(2) Å),  $\langle\text{Co2-O}\rangle$  (2.0640(17) Å), and  $\langle\text{Co3-O}\rangle$  (2.0810(16) Å). This indicates that the  $\text{CoO}_6$  octahedron is characterized by the shortest inter-ion distance and the highest regularity. This reflects the small ionic radius of the  $\text{Co}^{3+}$  ion in the low-spin state (LS) ( $t_{2g}^6 e_g^0$ ,  $S = 0$ ,  $r_i = 0.545$  Å), which occupies the crystallographic site 4. In contrast, high-spin (HS)  $\text{Co}^{2+}$  ions ( $t_{2g}^4 e_g^2$ ,  $S = 3/2$ ,  $r_i = 0.745$  Å) are found at sites 1, 2, and 3, contributing to ferrimagnetism [25].

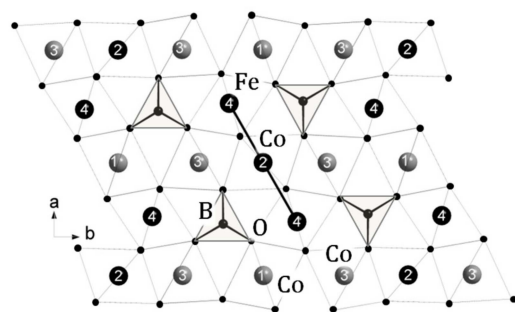


**Figure 1.** Crystal structure of  $\text{Co}_2\text{FeO}_2\text{BO}_3$  in the  $ab$ -plane. The structure comprises octahedra that correspond to divalent and trivalent metal ions positioned at non-equivalent crystallographic sites (1, 2, 3, and 4). Planar  $\text{BO}_3$  triangles are also illustrated. Black octahedra indicate  $(\text{Co}/\text{Fe})^{3+}\text{O}_6$ , with a specific emphasis on  $\text{FeO}_6$ , while gray octahedra represent continuous  $\text{Co}^{2+}\text{O}_6$  layers that interact through  $\text{BO}_3$  groups and  $\text{Fe}^{3+}\text{O}_6$  octahedra.

In  $\text{Co}_2\text{FeO}_2\text{BO}_3$ , the metal–oxygen interionic distances revealed that the  $(\text{Co}/\text{Fe})4\text{-O}$  bond is shorter at  $2.0666(14)$  Å compared to  $\langle\text{Co}1\text{-O}\rangle$  ( $2.1173(19)$  Å),  $\langle(\text{Co}/\text{Fe})2\text{-O}\rangle$  ( $2.0954(19)$  Å), and  $\langle\text{Co}3\text{-O}\rangle$  ( $2.1163(18)$  Å). These shorter average metal–oxygen bond lengths suggest higher valence  $\text{Fe}^{3+}$  ions ( $r_i = 0.645$  Å) compared to  $\text{Co}^{2+}$  ions ( $r_i = 0.745$  Å). It should be noted that mixed metal ion occupancy at crystallographic sites of 1, 2, 3, and 4 complicates the structure. Single-crystal X-ray diffraction shows that crystallographic sites 2 and 4 are occupied by  $\text{Co}(65.2\%)/\text{Fe}(34.8\%)$  and  $\text{Co}(21\%)/\text{Fe}(79\%)$ , respectively, while sites 1 and 3 are exclusively filled by  $\text{Co}$  [19]. It is important to note that non-resonant X-ray diffraction struggles to distinguish  $\text{Co}$  from  $\text{Fe}$  due to their similar atomic scattering factors, so it is reasonable to assume that  $\text{Fe}$  predominantly occupies site 4, which is also found to be energetically favored [27]. In this case, it is reasonable to propose that the structure consists of continuous  $\text{Co}^{2+}\text{O}_6$  layers lying in the  $bc$ -plane, linked along the  $a$ -axis through  $\text{BO}_3$  triangles and  $\text{Fe}^{3+}\text{O}_6$  octahedra.

The magnetic properties of  $\text{Co}_2\text{FeO}_2\text{BO}_3$  depend on its complex crystallography. Figure 2 shows a comparison of the macroscopic magnetic hysteresis curve (at 15 K) with element-selective magnetization curves along the  $b$ -axis, highlighting their impact on magnetic behavior. The shape of the loops suggests a mixture of ferromagnetic and antiferromagnetic contributions, where remagnetization proceeds through the motion of domain walls. Substituting  $\text{Co}$  with  $\text{Fe}$  increases the coercive field, achieving over 7 T for  $\text{Co}_2\text{FeO}_2\text{BO}_3$  below 15 K, surpassing those of  $\text{Nd}_{15.4}\text{Fe}_{77.8}\text{B}_{6.8}$  [29],  $\text{Nd}_2\text{Fe}_{14}\text{B}$  (5–6.5 T at 80 K) [30],  $\text{SmCo}_5$  (4.3 T at 4.2 K) [31],  $\text{Sm}_2\text{Co}_{17}$  (1.5–1.7 T at 4.2 K) [32]. The increased coercive field in  $\text{Co}_2\text{FeO}_2\text{BO}_3$  likely results from crystal defects caused by substituting inactive  $\text{Co}^{3+}$  ions with active  $\text{Fe}^{3+}$  ions.

Element-sensitive studies, such as XMCD, are crucial for analyzing this material, as they reveal its magnetic behaviors and spin dynamics [28].  $L$ -edge spectroscopy provides distinct benefits compared to  $K$ -edge spectroscopy, including sharper multiplet features and reduced core–hole lifetime broadening, even though  $K$ -edge spectroscopy offers deeper probing capabilities.  $L$ -edge studies are surface-sensitive, probing the top ~10 nm of the material.

Surface-sensitive XAS and XMCD at the  $\text{Co}$  and  $\text{Fe}$   $L_3$ -edges were performed on a  $\text{Co}_2\text{FeO}_2\text{BO}_3$  sample from 5 K to 130 K under a magnetic field of 6 T. The  $\text{Co}$   $L_3$  XAS spectrum (Figure S1) of  $\text{Co}_2\text{FeO}_2\text{BO}_3$  at 5 K shows a complex multiplet structure [33]. The primary features are observed at 776.6 eV, 777.93 eV, and 779.25 eV, aligning with those typical of HS  $\text{Co}^{2+}$  in solids. Analysis with reference spectra for HS  $\text{Co}^{3+}$ , LS  $\text{Co}^{3+}$ , and HS  $\text{Co}^{2+}$  [34] reveals that the spectrum consists solely of HS  $\text{Co}^{2+}$ . Thus, all  $\text{Co}$  ions in  $\text{Co}_2\text{FeO}_2\text{BO}_3$  are in the HS  $\text{Co}^{2+}$  state, with no LS  $\text{Co}^{3+}$  or HS  $\text{Co}^{3+}$  detected.

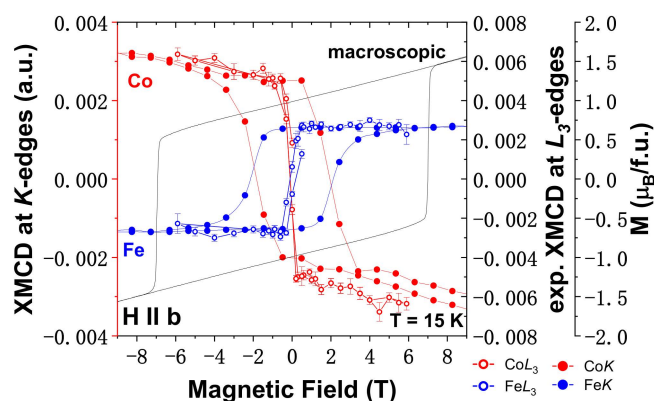


**Figure 2.** Comparison of macroscopic magnetic hysteresis curve (measured with  $H = \pm 9$  T) with element-selective magnetization curves for  $\text{Co}_2\text{FeO}_2\text{BO}_3$ , measured at 779.3 eV of the Co  $L_3$ -edge, at 710.3 eV of the Fe  $L_3$ -edge, at 7711.0 eV of the Co K-edge, at 7119.5 eV of the Fe K-edge along the  $b$ -axis.

The Fe  $L_3$  XAS spectrum (Figure S1b) exhibits a characteristic double peak often observed in oxides, resembling HS  $\text{Fe}^{3+}$  in hematite ( $\alpha\text{-Fe}_2\text{O}_3$ ) [35]. The Fe  $L_3$ -spectrum exhibits the primary features  $L_3$  and  $L_2$  at 708.43 eV, and 710.25 eV, respectively, corresponding to HS  $\text{Fe}^{3+}$  in solids. We performed charge transfer multiplet calculations to analyze the spectral shape of the experimental X-ray absorption spectra. For this purpose, we used the CTM4XAS program package [36], which is based on a semi-empirical approach including crystal field theory, core-hole effects, spin-orbit coupling, multiplet effects, and charge transfer.

For  $\text{Fe}^{3+}$  ions on octahedral sites, the best fit for the spectra was obtained with a crystal field splitting of  $10Dq = +1.8$  eV, with the values of the Slater integrals reduced to 80% of the atomic value, accounting for reduced Coulomb repulsion. For  $\text{Co}^{2+}$  ions, the crystal field was smaller due to the lower charge of the cation. We obtained  $10Dq = +1.2$  eV for the octahedral case, with the values of the Slater integrals reduced to approximately 90% of the atomic value. For all other quantities, corresponding atomic values were used. Lorentzian lifetime broadenings of 0.2 eV and 0.5 eV for the  $L_3$  and  $L_2$  absorption edges, respectively, were included. An additional Gaussian broadening of 0.1 eV accounts for the instrumental broadening. Thus, these calculations confirm the presence of HS  $\text{Co}^{2+}$  and HS  $\text{Fe}^{3+}$  states in  $\text{Co}_2\text{FeO}_2\text{BO}_3$ .

The XMCD spectrum of Fe exhibits a positive onset at the  $L_3$  peak (Figure S1b). Combined with the negative sign of the Co  $L_3$  XMCD in the same measurement geometry (Figure S1a), this indicates an antiferromagnetic coupling between the magnetic moments of the two constituents. The XMCD sign remains unchanged with temperature, and the asymptotic behavior is also conserved, indicating the stability of the electronic structure. Only the amplitude changes, reflecting temperature-induced variations in the magnetic moments. The absence of an inversion in the Fe and Co XMCD confirms that the coupling of the Fe and Co magnetic moments is a collinear antiferromagnetic configuration across the entire temperature range.

A quantitative analysis of the spin and orbital components contributing to the overall magnetic moment was carried out using well-established sum rules [37,38]. From the XMCD spectra, one can extract the orbital magnetic moment ( $m_L$ ) and the effective spin magnetic moment ( $m_S^{\text{eff}}$ ). The temperature dependencies of the orbital and spin moments for iron and cobalt are shown in Figure 3.

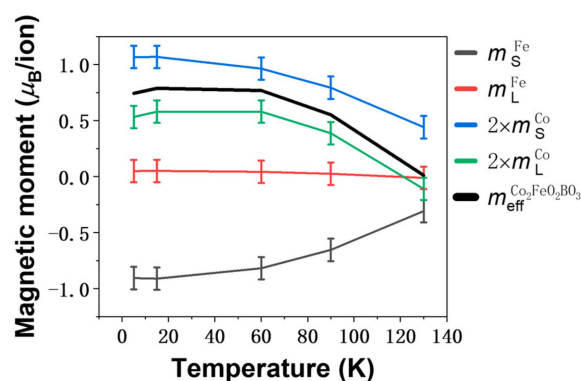


**Figure 3.** Orbital magnetic moments, effective spin magnetic moments, and total magnetic moment  $\text{Co}_2\text{FeO}_2\text{BO}_3$ , obtained via sum rules [37,38], as a function of temperature along the **b**-axis.

The cobalt orbital moment remains notably substantial and aligns with the spin moment, whereas in the iron sublattice, the spin magnetic moment exhibits a consistent negative orientation, being antiparallel to that of cobalt's spin moment. The XMCD data shows that the  $\text{Co}_2\text{FeO}_2\text{BO}_3$  system possesses a large unquenched orbital magnetic moment of Co, which contributes to the giant magnetic anisotropy. It also suggests a unique ferrimagnetic alignment of the  $\text{Co}^{2+}$  and  $\text{Fe}^{3+}$  spins. At 5 K, the magnetic orbital moment for Co was calculated to be  $0.27 \pm 0.1 \mu_B/\text{ion}$ , and the spin moment was  $0.53 \pm 0.1 \mu_B/\text{ion}$ , resulting in a total effective magnetic moment of  $0.80 \pm 0.1 \mu_B/\text{ion}$  for one cobalt atom. The orbital moments of Fe ions in  $\text{Co}_2\text{FeO}_2\text{BO}_3$  are very close to zero ( $0.05 \pm 0.1 \mu_B/\text{ion}$ ), as expected for  $\text{Fe}^{3+}$  with its half-filled d-shell ( $3d^5$ ). The spin moment was  $-0.90 \pm 0.1 \mu_B/\text{ion}$ , resulting in a total effective magnetic moment of  $-0.85 \pm 0.1 \mu_B/\text{ion}$ .

The effective spin moment can have a significant contribution from the intra-atomic spin dipole term  $\langle T_Z \rangle$ , related to aspherical spin density distributions. Note that for Co ions, a significant contribution of  $\langle T_Z \rangle$  may be present that does not average out due to the larger spin-orbit coupling. Thus, the resulting magnetic moment, defined as  $2 \times (m_L^{\text{Co}} + m_S^{\text{Co}}) - (m_L^{\text{Fe}} + m_S^{\text{Fe}}) = \sim 0.8 \mu_B/\text{f.u.}$  at 5 K, is close to that observed in macroscopic measurements with an experimental magnetic moment of approximately  $1.4 \mu_B/\text{f.u.}$  at 6 T (as seen in Figure 2) [19]. Therefore, we can conclude that the total magnetization is determined by the contributions of both subsystems to the magnetization of  $\text{Co}_2\text{FeO}_2\text{BO}_3$ . Unfortunately, within our accuracy limits, we could not reliably observe features that might be associated with magnetic transitions at 70 K, which is observed in this sample along the **b**-axis [19].

Moreover, it is worth noting that according to recent DFT calculations [27], the total magnetic moment of the Co sublattice along the **b**-axis was determined to be  $+2.5 \mu_B$ , while the magnetic moment of the Fe sublattice was  $-3.6 \mu_B$ , and it is oppositely directed. The orbital moments were parallel to the spin moments:  $\sim 0.15\text{--}0.30 \mu_B$  for Co ions and  $\sim 0.06 \mu_B$  for Fe ions [27]. The differences in the total magnetic moments from those obtained using DFT are likely due to the dielectric nature of the samples, which ultimately distorts the XAS spectrum, despite all our measurements being in agreement with the macroscopic data.

Additionally, the strong covalent bonding between B and O atoms suggests that the  $\text{BO}_3$  unit acts as a rigid structure, contributing to the stability of the crystal. A qualitative experimental indication of this stability can be observed at the oxygen *K*-edge [39–41]. In Figure S3, we present the O *K*-edge XAS spectrum measured at 6 T and 5 K. The O *K*-edge XAS reflects electron transitions from the O 1s core level to O 2p unoccupied states that are hybridized with the orbitals of neighboring Co/Fe ions. The lower energy range (529–535 eV) represents the Co/Fe 3d state hybridized with O 2p, while the higher energy range (535–545 eV) corresponds to the Co/Fe 4sp states hybridized with O 2p. The main absorption peaks in the energy range of 535–554 eV correspond to oxygen 2p states

hybridized with the 4p and 4s states of the transition metal cations. More relevant in the present context are the absorption peaks in the pre-edge region around 530–532 eV, which correspond to electron transitions into oxygen 2p states hybridized with 3d states.

Analysis of the oxygen spectrum indicates that there are also 4sp orbitals from iron and cobalt involved in covalent bonding; i.e., there are 4sp from the transition metal involved in the covalency. Unfortunately, the XMCD signal from oxygen was very noisy; however, a small magnetic signal was still detectable. This may indicate that oxygen is magnetic due to super-exchange interactions.

Field-dependent and temperature-dependent XMCD measurements at the maximum XMCD signal energies for Co and Fe ions were performed to trace the magnetic sublattice contributions to overall magnetization and determine the origin of the large magnetic stiffness. First, we examine the data obtained at the *L*-edges. Figure 2 presents the Co and Fe element-selective hysteresis loops in  $\text{Co}_2\text{FeO}_2\text{BO}_3$ , measured at the  $L_3$ -edges under an applied magnetic field oriented along the **b**-axis at 5 K. The distinct XMCD signals confirm antiparallel magnetic sublattices, with amplitudes corresponding to the ratio of elements in the formula  $\text{Co}/\text{Fe} = 2/1$ . The slope of the Co XMCD loop suggests that antiferromagnetic interactions at Co sites are more pronounced compared to those at Fe sites. The Co  $L_3$ -edge XMCD loop exhibits a coercive field near 0.1 T, whereas that of the Fe  $L_3$ -edge is approximately 0.145 T. This differs significantly from the hysteresis measured at 15 K using macroscopic magnetization measurements. Surface effects, such as strain and defects, likely cause variations in measured coercive fields due to the shallow escape depth (less than 10 nm).

To further verify the small value of coercivity obtained from the Co and Fe *L*-edge measurements, we performed measurements in the hard X-ray region at the *K*-edges of X-ray absorption. Hard X-rays at the *K*-edge penetrate up to approximately 10 microns, allowing for bulk property analysis that extends beyond the surface sensitivity typically associated with *L*-edge XAS. Before discussing the field dependencies from the XANES/XMCD spectra measurements at the *K*-edges, it should be noted that we recently proposed a method for isolating the contributions of different valence subsystems of cobalt in  $\text{Co}_3\text{O}_2\text{BO}_3$  [25] and additionally confirmed the presence of HS  $\text{Co}^{2+}$  and HS  $\text{Fe}^{3+}$ . A detailed description of this method is provided in the Supplementary Materials.

Figure 2 also shows the magnetization curves obtained through element-selective measurements for  $\text{Co}_2\text{FeO}_2\text{BO}_3$  at Co (7711.0 eV) and Fe (7119.5 eV), recorded near their pre-*K* edges at 15 K with an applied field of  $\pm 17$  T along the **b**-axis. The XMCD data for cobalt and iron clearly show hysteresis behavior. At 15 K, these element-selective loops show notable coercivity, though it remains lower than the values detected in the bulk macroscopic experiments.

Fe magnetization measured at the *K*-absorption edge is close to the saturation state, indicating ferromagnetic ordering of  $\text{Fe}^{3+}$  moments. Co magnetization tilts in high fields, suggesting mixed antiferromagnetic and ferromagnetic contributions, which are characteristic of  $\text{Co}^{2+}$  ferrimagnetic ordering in  $\text{Co}_2\text{FeO}_2\text{BO}_3$ . These contributions from AFM and ferromagnetic Co are experimentally observed at the Co  $L_3$ -edge (Figure S2a,b), while the XMCD Fe  $L_3$ -edge is always in the saturation state, indicating the presence of only one contribution.

Temperature-dependent behavior of the Co and Fe magnetic sublattices in  $\text{Co}_2\text{FeO}_2\text{BO}_3$  was investigated by analyzing measurements at the  $L_3$ - and *K*-edges, in comparison with macroscopic magnetization data recorded at 5 T along the **b**-axis (Figure S4). XMCD signals peak around 70 K, consistent with macroscopic magnetization data, and reveal magnetic coupling between the Co and Fe subsystems, contrary to earlier interpretations suggesting that these subsystems act independently in similar compounds [13,21,42,43].

Throughout the temperature range, the oppositely directed hysteresis loops for Co and Fe indicate the antiferromagnetic nature of the  $\text{Co}^{2+}$ -O- $\text{Fe}^{3+}$  exchange interaction, suggesting different contributions from each subsystem to the total magnetization. Element-selective magnetization of Co in  $\text{Co}_2\text{FeO}_2\text{BO}_3$  shows that the  $\text{Co}^{2+}$  magnetic subsystem primarily determines the total magnetization due to its significant orbital moment ( $m_L$ ). At low temperatures,  $m_L$  orientation is determined by both the magnetic field ( $H$ ) and intraatomic spin-orbit coupling ( $H_{LS}$ ), which, according to Hund's third rule, favors parallel alignment of the orbital ( $m_L$ ) and spin ( $m_S$ ) moments. The exchange field ( $H_{\text{ex}}^{\text{Fe-Co}}$ ) at low temperatures tends to align Fe moments antiparallel to Co and, hence, to the external field, leading to magnetic moment compensation along the  $\mathbf{b}$ -axis from  $M_r = 3.5 \mu_B/\text{f.u.}$  for  $\text{Co}_3\text{O}_2\text{BO}_3$  [19] to  $\sim 1.5 \mu_B/\text{f.u.}$  for  $\text{Co}_2\text{FeO}_2\text{BO}_3$  (Figure 2). Thus, the metal ion at crystallographic site 4 critically determines the magnetic state [25]. These results are supported by magnetization [19], heat capacity [13], Mössbauer effect [27], and DFT calculations [27], which show an almost collinear spin configuration  $1(\downarrow)2(\uparrow)3(\uparrow)4(\downarrow)$  with  $\text{Fe}^{3+}$  ( $d^5$ , HS) at site 4 and  $\text{Co}^{2+}$  ( $d^7$ , HS) at sites 1, 2, and 3.

Figure 4, which represents the temperature variation in the measured element-selective XMCD hysteresis loop area, shows a significant reduction in coercivity (and so small compared to the macroscopic) measured by XMCD for the Co and Fe sublattices. In  $\text{Co}_2\text{FeO}_2\text{BO}_3$ , the element-selective  $H_C$  areas peak at 15 K as the temperature decreases from 60 K, indicating strong magnetic coupling between these sublattices. This behavior is consistent with the magnetic measurements on the  $\text{Ni}_2\text{FeO}_2\text{BO}_3$  sample in [13], where this effect was first detected. The origin of the temperature dependence of coercivity in each case should reflect the compromise of the temperature dependence for all the magnetic anisotropy energy contributions, namely magnetoelastic, magnetocrystalline and shape or magnetostatic terms.

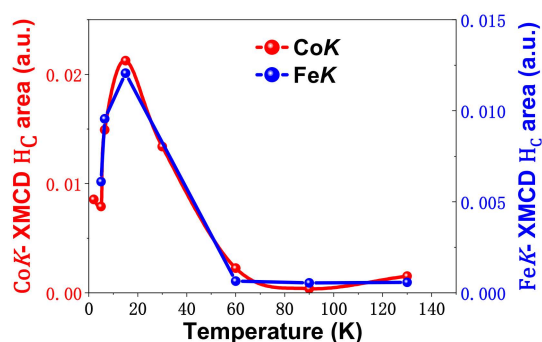


**Figure 4.** Temperature-dependent CoK- and FeK-edge XMCD  $H_C$  areas for  $\text{Co}_2\text{FeO}_2\text{BO}_3$ , measured across a temperature range of 5 to 130 K.

In  $\text{Co}_2\text{FeO}_2\text{BO}_3$ , the transition at  $T_{N2} = 70$  K is metamagnetic, consistent with magnetic susceptibility measurements showing a frequency-dependent peak indicative of domain wall motion in ferrimagnetic domains, which slightly shifts to higher temperatures with increasing frequency [20]. The increase in the magnetic transition temperature and Curie–Weiss temperature indicates a rise in exchange energy ( $A$ ) in  $\text{Co}_2\text{FeO}_2\text{BO}_3$  compared to  $\text{Co}_3\text{O}_2\text{BO}_3$ , but this alone does not explain the increased coercivity ( $H_C$ ). If the anisotropy constant ( $K$ ) remains the same due to identical  $\text{Co}^{2+}$  ion concentration and distribution, the primary cause of the increased  $H_C$  is the higher defect density introduced by  $\text{Fe}^{3+}$  ions, which significantly reduces the average distance between magnetic domains [19].

In  $\text{Nd}_2\text{Fe}_{14}\text{B}$ -based magnets, the coercive field is significantly affected by factors such as soft magnetic grain boundaries, misalignment of the anisotropy axes [44,45], and structural imperfections [44,46]. These elements account for approximately 60% of the reduction, while internal demagnetizing fields and temperature-driven fluctuations contribute an

additional 18%. Our study demonstrates a reduction exceeding 70%, suggesting the influence of other contributing mechanisms. Non-uniformly demagnetizing fields may lead to uneven magnetization reversal, thereby impacting element-selective coercivity. For  $\text{Co}_2\text{FeO}_2\text{BO}_3$ , these effects should not exceed 3%. Local self-demagnetizing fields at single sites, initiating reversed domain nucleation [47], contribute significantly, as observed in mixed cobalt–zinc ferrite nanoparticles [48], where cationic distribution and spin-canting reduce coercivity. The significant difference between local and bulk coercive fields suggests domain walls are bound to crystallographic sites, contributing to high bulk coercivity.

The coercivity of magnetic materials usually increases as the domain wall width ( $\delta$ ) decreases, due to enhanced pinning from defects, impurities, and grain boundaries, following the relation  $H_C \propto 1/\delta$  [49]. In  $\text{Co}_2\text{FeO}_2\text{BO}_3$ , variations in coercivity with temperature can be attributed to a domain wall pinning mechanism influenced by changes in the anisotropy field and thermally activated domain wall motion, where magnetocrystalline anisotropy plays a crucial role [50]. We performed an estimation of the domain wall width ( $\delta$ ), which is presented in Figure S6.  $\text{Co}_2\text{FeO}_2\text{BO}_3$ , a multi-sublattice ferrimagnet, shows similar local coercivity fields (signals differ in Figure 4 by a factor of two due to the different elemental content  $\text{Co}/\text{Fe} = 2/1$ ), indicating comparable anisotropy constants for the cobalt and iron sublattices [20]. The calculated temperature-dependent domain wall widths, which are less than 1 nm, are comparable to the lattice constant  $\mathbf{b}$  and the metal–metal distance 4–2 (~0.3 nm) [19], but are smaller than those for Sm–Co-based magnets (1–3 nm) [51,52]. Recently, atomically sharp domain walls under 1 nm were directly observed in CuMnAs films [53], suggesting similar domain walls may exist in our samples. Thus, the high coercivity of  $\text{Co}_2\text{FeO}_2\text{BO}_3$  can be attributed to significant pinning effects, high magnetic anisotropy, and domain wall dynamics.

#### 4. Conclusions

In conclusion, this study shows that  $\text{Co}_2\text{FeO}_2\text{BO}_3$ , a lanthanide-free multi-sublattice ferrimagnet, exhibits exceptional magnetic properties, particularly its extremely high coercivity. These properties arise from charge-ordering and the distinctive spatial distribution of magnetic ions in its crystal lattice. The specific cation arrangement significantly impacts the magnetic behavior of ludwigites by altering the anisotropic energy landscape and creating localized barriers that impede domain wall motion, thereby enhancing coercivity.

Element-selective XMCD analysis reveals that Co and Fe contribute to the total magnetization in a temperature-dependent manner, with  $\text{Co}^{2+}$ -O- $\text{Fe}^{3+}$  antiferromagnetic interactions occurring across the entire temperature range. The XMCD experiments show that while the magnetization of Fe nears saturation at low temperatures, Co exhibits both antiferromagnetic and ferromagnetic contributions. This suggests a magnetic structure comprising infinite  $\text{Co}^{2+}\text{O}_6$  layers in the  $\mathbf{bc}$ -plane, with strong antiferromagnetic coupling through  $\text{Fe}^{3+}$  ions.

We propose that controlling the substitution of specific inequivalent crystallographic sites, which act as pinning centers for domain walls, can help create materials with high coercivity. These sites may exhibit different magnetic anisotropies, and substituting atoms in these locations can modify local anisotropy, creating regions with high energy barriers for domain wall movement. By optimizing the composition and substitution of atoms at these sites, it is possible to enhance the magnetic properties of lanthanide-free materials, resulting in high-coercivity materials suitable for various applications.

Lanthanide-free magnetic materials, such as  $\text{Co}_2\text{FeO}_2\text{BO}_3$ , represent a class of sustainable alternatives to rare-earth-based magnets. Other examples include  $\text{SrFe}_{12}\text{O}_{19}$  (strontium ferrites), which are widely used in low-cost permanent magnets, and  $\text{Fe}_3\text{O}_4$  (magnetite), known for its excellent magnetic performance in specific applications. These

materials demonstrate the possibility of achieving desirable magnetic properties, such as high coercivity and strong magnetic anisotropy, without relying on rare-earth elements. Their development is particularly significant for addressing global challenges in resource availability and the environmental impact of rare-earth mining and processing.

In summary, this research highlights  $\text{Co}_2\text{FeO}_2\text{BO}_3$  as an example of a promising lanthanide-free magnetic material, offering insights into the design principles that could guide the development of other advanced magnets.

**Supplementary Materials:** The following supporting information can be downloaded at: <https://www.mdpi.com/article/10.3390/inorganics13010024/s1>.

**Funding:** This work was supported by the Ministry of Science and Higher Education of the Russian Federation (Agreement No. 075-15-2022-263).

**Data Availability Statement:** The datasets generated and analyzed during this study, including the raw spectra, are available from the corresponding author upon reasonable request.

**Acknowledgments:** The author deeply appreciates the late L.N. Bezmaternykh for synthesizing the  $\text{Co}_2\text{FeO}_2\text{BO}_3$  sample and for his insightful discussions that shaped this work. This study explores controlling magnetic interactions in charge-ordered, lanthanide-free materials, inspired by Bezmaternykh's ideas. The authors also thank colleagues and co-authors from previous collaborations: J. Bartolome, S. G. Ovchinnikov, A. Rogalev, F. Wilhelm, the late N.B. Ivanova, and others for their discussions. Gratitude is also extended to ESRF and BESSY II for the provision of beamtime and staff support. X-ray diffraction (A. Vasiliev) and magnetization measurements (E. Eremin) were performed at the Common Access Facility Centres of SB RAS in Krasnoyarsk, Russia. The investigations were performed using the large-scale research facility 'EXAFS Spectroscopy Beamline' at the Siberian Synchrotron and Terahertz Radiation Center in Novosibirsk, Russia.

**Conflicts of Interest:** The author declares that they have no known competing financial interests or personal relationships that could appear to have influenced the work reported in this paper.

## References

1. Gutfleisch, O.; Willard, M.A.; Brück, E.; Chen, C.H.; Sankar, S.G.; Liu, J.P. Magnetic materials and devices for the 21st century: Stronger, lighter, and more energy efficient. *Adv. Mater.* **2011**, *23*, 821–842. [[CrossRef](#)] [[PubMed](#)]
2. Chu, S.; Majumdar, A. Opportunities and challenges for a sustainable energy future. *Nature* **2012**, *488*, 294–303. [[CrossRef](#)] [[PubMed](#)]
3. Bollero, A.; Palmero, E.M. Recent advances in hard ferrite magnets. *Mod. Perm. Magn.* **2022**, *3*, 65–112. [[CrossRef](#)]
4. Kwon, H.; McClain, K.R.; Kragoskow, J.G.C.; Staab, J.K.; Ozerov, M.; Meihaus, K.R.; Harvey, B.G.; Choi, E.S.; Chilton, N.F.; Long, J.R. Coercive fields exceeding 30 T in the mixed-valence single-molecule magnet  $(\text{Cp}^*\text{Pr}_5)_2\text{Ho}_2\text{I}_3$ . *J. Am. Chem. Soc.* **2024**, *146*, 18714–18721. [[CrossRef](#)] [[PubMed](#)]
5. Perlepe, P.; Oyarzabal, I.; Mailman, A.; Yquel, M.; Platunov, M.; Dovgaliuk, I.; Rouzières, M.; Négrier, P.; Mondieig, D.; Sutura, E.A.; et al. Metal-organic magnets with large coercivity and ordering temperatures up to 242 °C. *Science* **2020**, *370*, 587–592. [[CrossRef](#)]
6. Miller, J.S. Organic-and molecule-based magnets. *Mater. Today* **2014**, *17*, 224–235. [[CrossRef](#)]
7. Goodwin, C.A.P.; Ortu, F.; Reta, D.; Chilton, N.F.; Mills, D.P. Molecular magnetic hysteresis at 60 kelvin in dysprosocenium. *Nature* **2017**, *548*, 439–442. [[CrossRef](#)]
8. Guo, F.-S.; Day, B.M.; Chen, Y.-C.; Tong, M.-L.; Mansikkamäki, A.; Layfield, R.A. Magnetic hysteresis up to 80 kelvin in a dysprosium metallocene single-molecule magnet. *Science* **2018**, *362*, 1400–1403. [[CrossRef](#)]
9. Coey, M. Charge-ordering in oxides. *Nature* **2004**, *430*, 155–157. [[CrossRef](#)]
10. Mir, M.; Guimarães, R.B.; Fernandes, J.C.; Continentino, M.A.; Doriguetto, A.C.; Mascarenhas, Y.P.; Ellena, J.; Castellano, E.E.; Freitas, R.S.; Ghivelder, L. Structural transition and pair formation in  $\text{Fe}_3\text{O}_2\text{BO}_3$ . *Phys. Rev. Lett.* **2001**, *87*, 147201. [[CrossRef](#)]
11. Galdino, C.W.; Freitas, D.C.; Medrano, C.P.C.; Tartaglia, R.; Rigitano, D.; Oliveira, J.F.; Mendonça, A.A. Magnetic, electronic, structural, and thermal properties of the  $\text{Co}_3\text{O}_2\text{BO}_3$  ludwigite in the paramagnetic state. *Phys. Rev. B* **2019**, *100*, 165138. [[CrossRef](#)]
12. Larrea, J.; Sánchez, D.R.; Litterst, F.J.; Baggio-Saitovitch, E.M.; Fernandes, J.C.; Guimaraes, R.B.; Continentino, M.A. Magnetism and charge ordering in  $\text{Fe}_3\text{O}_2\text{BO}_3$  studied by  $\text{Fe}^{57}$  Mössbauer spectroscopy. *Phys. Rev. B* **2004**, *70*, 174452. [[CrossRef](#)]

13. Freitas, D.C.; Continentino, M.A.; Guimaraes, R.B.; Fernandes, J.C.; Oliveira, E.P.; Santelli, R.E.; Ellena, J.; Eslava, G.G.; Ghivelder, L. Partial magnetic ordering and crystal structure of the ludwigites  $\text{Co}_2\text{FeO}_2\text{BO}_3$  and  $\text{Ni}_2\text{FeO}_2\text{BO}_3$ . *Phys. Rev. B* **2009**, *79*, 134437. [[CrossRef](#)]
14. Kumar, J.; Panja, S.N.; Mukkattukavil, D.J.; Bhattacharyya, A.; Nigam, A.K.; Nair, S. Reentrant superspin glass state and magnetization steps in the oxyborate  $\text{Co}_2\text{AlBO}_5$ . *Phys. Rev. B* **2017**, *95*, 144409. [[CrossRef](#)]
15. Heringer, M.A.V.; Mariano, D.L.; Freitas, D.C.; Baggio-Saitovitch, E.; Continentino, M.A.; Sanchez, D.R. Spin-glass behavior in  $\text{Co}_3\text{Mn}_3(\text{O}_2\text{BO}_3)_2$  ludwigite with weak disorder. *Phys. Rev. Mater.* **2020**, *4*, 064412. [[CrossRef](#)]
16. Kulbakov, A.A.; Sarkar, R.; Janson, O.; Dengre, S.; Weinhold, T.; Moshkina, E.M.; Portnichenko, P.Y. Destruction of long-range magnetic order in an external magnetic field and the associated spin dynamics in  $\text{Cu}_2\text{GaBO}_5$  and  $\text{Cu}_2\text{AlBO}_5$  ludwigites. *Phys. Rev. B* **2021**, *103*, 024447. [[CrossRef](#)]
17. Medrano, C.P.C.; Sadrollahi, E.; Da Fonseca, R.G.M.; Passamani, E.C.; Freitas, D.C.; Continentino, M.A.; Sanchez, D.R.; Litterst, F.J.; Baggio-Saitovitch, E. Magnetic properties of  $\text{Ni}_5\text{Sn}(\text{O}_2\text{BO}_3)_2$  ludwigite. *Phys. Rev. B* **2021**, *103*, 064430. [[CrossRef](#)]
18. Damay, F.; Sottmann, J.; Fauth, F.; Suard, E.; Maignan, A.; Martin, C. High temperature spin-driven multiferroicity in ludwigite chromocuprate  $\text{Cu}_2\text{CrBO}_5$ . *Appl. Phys. Lett.* **2021**, *118*, 192903. [[CrossRef](#)]
19. Ivanova, N.B.; Kazak, N.V.; Knyazev, Y.V.; Velikanov, D.A.; Bezmaternykh, L.N.; Ovchinnikov, S.G.; Vasiliev, A.D.; Platunov, M.S.; Bartolomé, J.; Patrin, G.S. Crystal structure and magnetic anisotropy of ludwigite  $\text{Co}_2\text{FeO}_2\text{BO}_3$ . *J. Exp. Theor. Phys.* **2011**, *113*, 1015–1024. [[CrossRef](#)]
20. Bartolomé, J.; Arauzo, A.; Kazak, N.V.; Ivanova, N.B.; Ovchinnikov, S.G.; Knyazev, Y.V.; Lyubutin, I.S. Uniaxial magnetic anisotropy in  $\text{Co}_{2.25}\text{Fe}_{0.75}\text{O}_2\text{BO}_3$  compared to  $\text{Co}_3\text{O}_2\text{BO}_3$  and  $\text{Fe}_3\text{O}_2\text{BO}_3$  ludwigites. *Phys. Rev. B* **2011**, *83*, 144426. [[CrossRef](#)]
21. Bordet, P.; Suard, E. Magnetic structure and charge ordering in  $\text{Fe}_3\text{BO}_5$ : A single-crystal x-ray and neutron powder diffraction study. *Phys. Rev. B* **2009**, *79*, 144408. [[CrossRef](#)]
22. Freitas, D.C.; Continentino, M.A.; Guimaraes, R.B.; Fernandes, J.C.; Ellena, J.; Ghivelder, L. Structure and magnetism of homometallic ludwigites:  $\text{Co}_3\text{O}_2\text{BO}_3$  versus  $\text{Fe}_3\text{O}_2\text{BO}_3$ . *Phys. Rev. B* **2008**, *77*, 184422. [[CrossRef](#)]
23. Angst, M.; Hermann, R.P.; Schweika, W.; Kim, J.W.; Khalifah, P.; Xiang, H.J.; Whangbo, M.H.; Kim, D.H.; Sales, B.C.; Mandrus, D. Incommensurate charge order phase in  $\text{Fe}_2\text{OBO}_3$  due to geometrical frustration. *Phys. Rev. Lett.* **2007**, *99*, 256402. [[CrossRef](#)] [[PubMed](#)]
24. Freitas, D.C.; Medrano, C.P.C.; Sanchez, D.R.; Regueiro, M.N.; Rodríguez-Velamazán, J.A.; Continentino, M.A. Magnetism and charge order in the ladder compound  $\text{Co}_3\text{O}_2\text{BO}_3$ . *Phys. Rev. B* **2016**, *94*, 174409. [[CrossRef](#)]
25. Kazak, N.V.; Platunov, M.S.; Knyazev, Y.V.; Molokeev, M.S.; Gorev, M.V.; Ovchinnikov, S.G.; Pchelkina, Z.V. Spin state crossover in  $\text{Co}_3\text{BO}_5$ . *Phys. Rev. B* **2021**, *103*, 094445. [[CrossRef](#)]
26. Galdino, C.W.; Freitas, D.C.; Medrano, C.P.C.; Sanchez, D.R.; Tartaglia, R.; Rabello, L.P.; Mendonça, A.A. Structural and spectroscopic investigation of the charge-ordered, short-range ordered, and disordered phases of the  $\text{Co}_3\text{O}_2\text{BO}_3$  ludwigite. *Phys. Rev. B* **2021**, *104*, 195151. [[CrossRef](#)]
27. Knyazev, Y.V.; Kazak, N.V.; Zhandun, V.S.; Bartolomé, J.; Arauzo, A.; Belskaya, N.A.; Bayukov, O.A.; Bezmaternykh, L.N.; Ovchinnikov, S.G. Electronic and magnetic states of Fe ions in  $\text{Co}_2\text{FeBO}_5$ . *Dalton Trans.* **2021**, *50*, 9735–9745. [[CrossRef](#)]
28. Stöhr, J. Exploring the microscopic origin of magnetic anisotropies with X-ray magnetic circular dichroism (XMCD) spectroscopy. *J. Magn. Magn. Mater.* **1999**, *200*, 470–497. [[CrossRef](#)]
29. Kawai, T.; Ma, B.M.; Sankar, S.G.; Wallace, W.E. Effect of crystal alignment on the remanence of sintered NdFeB magnets. *J. Appl. Phys.* **1990**, *67*, 4610–4612. [[CrossRef](#)]
30. Cardarelli, F. *Materials Handbook*, 2nd ed.; Springer: London, UK, 2008. [[CrossRef](#)]
31. Kütterer, R.; Hilzinger, H.-R.; Kronmüller, H. The temperature dependence of the coercive field of  $\text{Co}_5\text{Sm}$  magnets. *J. Magn. Magn. Mater.* **1977**, *4*, 1–7. [[CrossRef](#)]
32. Tellez-Blanco, J.C.; Kou, X.C.; Grössinger, R.; Estevez-Rams, E.; Fidler, J.; Ma, B.M. Coercivity and magnetic anisotropy of sintered  $\text{Sm}_2\text{Co}_{17}$ -type permanent magnets. *J. Appl. Phys.* **1997**, *82*, 3928–3933. [[CrossRef](#)]
33. De Groot, F. High-resolution X-ray emission and X-ray absorption spectroscopy. *Chem. Rev.* **2001**, *101*, 1779–1808. [[CrossRef](#)] [[PubMed](#)]
34. Liu, J.; Si, L.; Zhang, Q.; Wang, X.; Freese, J.; Harris, G.; Wu, M.; Zhang, X.; Lin, T.; Sutarto, R.; et al. Realization of fully high-spin state and strong ferromagnetism in  $\text{LaCoO}_3$  monolayer. *Adv. Funct. Mater.* **2024**, 2401859. [[CrossRef](#)]
35. Brotton, S.J.; Shapiro, R.; van der Laan, G.; Guo, J.; Glans, P.A.; Ajello, J.M. Valence state fossils in Proterozoic stromatolites by *L*-edge X-ray absorption spectroscopy. *J. Geophys. Res. Biogeosci.* **2007**, *112*, G03004. [[CrossRef](#)]
36. Stavitski, E.; De Groot, F.M.F. The CTM4XAS program for EELS and XAS spectral shape analysis of transition metal *L* edges. *Micron* **2010**, *41*, 687–694. [[CrossRef](#)]
37. Carra, P.; Thole, B.T.; Altarelli, M.; Wang, X. X-ray circular dichroism and local magnetic fields. *Phys. Rev. Lett.* **1993**, *70*, 694. [[CrossRef](#)]

38. Thole, B.T.; Carra, P.; Sette, F.; van der Laan, G. X-ray circular dichroism as a probe of orbital magnetization. *Phys. Rev. Lett.* **1992**, *68*, 1943. [[CrossRef](#)]
39. De Groot, F.M.F.; Grioni, M.; Fuggle, J.C.; Ghijsen, J.; Sawatzky, G.A.; Petersen, H. Oxygen 1s X-ray absorption edges of transition-metal oxides. *Phys. Rev. B* **1989**, *40*, 5715. [[CrossRef](#)]
40. Colliex, C.; Manoubi, T.; Ortiz, C. Electron-energy-loss-spectroscopy near-edge fine structures in the iron-oxygen system. *Phys. Rev. B* **1991**, *44*, 11402. [[CrossRef](#)]
41. Pong, W.F.; Su, M.H.; Tsai, M.H.; Hsieh, H.H.; Pieh, J.Y.; Chang, Y.K.; Kuo, K.C.; Tseng, P.K.; Lee, J.F.; Chung, S.C.; et al. Oxygen 1s X-ray absorption near-edge structure of Zn-Ni ferrites: A comparison with the theoretical calculations. *Phys. Rev. B* **1996**, *54*, 16641. [[CrossRef](#)]
42. Fernandes, J.C.; Guimaraes, R.B.; Continentino, M.A.; Borges, H.A.; Sulpice, A.; Tholence, J.L.; Siqueira, J.L.; Zawislak, L.I.; Da Cunha, J.B.M.; Santos, C.A.D. Magnetic interactions in the ludwigite  $\text{Ni}_2\text{FeO}_2\text{BO}_3$ . *Phys. Rev. B* **1998**, *58*, 287. [[CrossRef](#)]
43. Continentino, M.A.; Fernandes, J.C.; Guimarães, R.B.; Borges, H.A.; Sulpice, A.; Tholence, J.-L.; Siqueira, J.L.; Da Cunha, J.B.M.; Santos, C.A.D. Magnetic interactions in the monoclinic ludwigite  $\text{Cu}_2\text{FeO}_2\text{BO}_3$ . *Eur. Phys. J. B* **1999**, *9*, 613–618. [[CrossRef](#)]
44. Hrkac, G.; Woodcock, T.G.; Butler, K.T.; Saharan, L.; Bryan, M.T.; Schrefl, T.; Gutfleisch, O. Impact of different Nd-rich crystal-phases on the coercivity of Nd-Fe-B grain ensembles. *Scr. Mater.* **2014**, *70*, 35–38. [[CrossRef](#)]
45. Kulesh, N.; Bolyachkin, A.; Dengina, E.; Tang, X.; Ohkubo, T.; Kajiwara, T.; Miyawaki, H.; Sepehri-Amin, H.; Hono, K. Coercivity limits in Nd-Fe-B hot-deformed magnets with ultrafine microstructure. *Acta Mater.* **2024**, *276*, 120159. [[CrossRef](#)]
46. Woodcock, T.G.; Zhang, Y.; Hrkac, G.; Ciuta, G.; Dempsey, N.M.; Schrefl, T.; Gutfleisch, O.; Givord, D. Understanding the microstructure and coercivity of high-performance NdFeB-based magnets. *Scr. Mater.* **2012**, *67*, 536–541. [[CrossRef](#)]
47. Bance, S.; Seebacher, B.; Schrefl, T.; Exl, L.; Winklhofer, M.; Hrkac, G.; Zimanyi, G.; Shoji, T.; Yano, M.; Sakuma, N.; et al. Grain-size dependent demagnetizing factors in permanent magnets. *J. Appl. Phys.* **2014**, *116*, 233903. [[CrossRef](#)]
48. Fischbacher, J.; Kovacs, A.; Exl, L.; Kühnel, J.; Mehofer, E.; Sepehri-Amin, H.; Ohkubo, T.; Hono, K.; Schrefl, T. Searching the weakest link: Demagnetizing fields and magnetization reversal in permanent magnets. *Scr. Mater.* **2018**, *154*, 253–258. [[CrossRef](#)]
49. Bishop, A.R.; Lewis, W.F. A theory of intrinsic coercivity in narrow magnetic domain wall materials. *J. Phys. C Solid State Phys.* **1979**, *12*, 3811. [[CrossRef](#)]
50. Guo, X.; Chen, X.; Altounian, Z.; Ström-Olsen, J.O. Temperature dependence of coercivity in MnBi. *J. Appl. Phys.* **1993**, *73*, 6275–6277. [[CrossRef](#)]
51. Hubert, A. *Schäfer, Magnetic Domains*, 1st ed.; Springer: Berlin/Heidelberg, Germany, 1998. [[CrossRef](#)]
52. Duerrschabel, M.; Yi, M.; Üstüner, K.; Liesegang, M.; Katter, M.; Kleebe, H.-J.; Xu, B.; Gutfleisch, O.; Molina-Luna, L. Atomic structure and domain wall pinning in samarium-cobalt-based permanent magnets. *Nat. Commun.* **2017**, *8*, 54. [[CrossRef](#)]
53. Krizek, F.; Reimers, S.; Kašpar, Z.; Marmodoro, A.; Michalička, J.; Man, O.; Edström, A.; Amin, O.J.; Edmonds, K.W.; Campion, R.P.; et al. Atomically sharp domain walls in an antiferromagnet. *Sci. Adv.* **2022**, *8*, eabn3535. [[CrossRef](#)]

**Disclaimer/Publisher's Note:** The statements, opinions and data contained in all publications are solely those of the individual author(s) and contributor(s) and not of MDPI and/or the editor(s). MDPI and/or the editor(s) disclaim responsibility for any injury to people or property resulting from any ideas, methods, instructions or products referred to in the content.